

# High-Temperature Synthesis of Nickel-Based Nanoparticles for Use as Materials in Sensors of Potentially Hazardous Gases

P. Tarttelin Hernández<sup>a, \*</sup>, M. V. Kuznetsov<sup>b, \*\*</sup>, and Yu. G. Morozov<sup>c, \*\*\*</sup>

<sup>a</sup>*School of Life Sciences, Coventry University, Priory Street, Coventry, CV1 5FB United Kingdom*

<sup>b</sup>*All-Russia Research Institute on Problems of Civil Defense and Emergencies, Emergency Control Ministry (EMERCOM), Moscow, 121352 Russia*

<sup>c</sup>*Merzhanov Institute of Structural Macrokinetics and Materials Science, Russian Academy of Sciences, Chernogolovka, Moscow, 142432 Russia*

\**e-mail: ad0561@coventry.ac.uk*

\*\**e-mail: maxim1968@mail.ru*

\*\*\**e-mail: morozov@ism.ac.ru*

Received October 11, 2018; revised December 17, 2018; accepted December 29, 2018

**Abstract**—The gas-sensing properties of nickel ferrite (NiFe<sub>2</sub>O<sub>4</sub>) and nickel oxide (NiO) nanoparticles prepared by a self-sustaining levitation-jet synthesis (LJS) method are reported. These have been compared to the gas-sensing properties of a NiO sensor prepared using a commercially sourced powder. The microstructure, surface area, particle size, and morphology varied widely across the sensors fabricated. It was anticipated that these contrasting properties would play a key role in either enhancing or worsening the sensing capabilities of the materials. Gases of interest included ethanol, toluene, and carbon monoxide as well as the gas response of the sensors was investigated at different operating temperatures. In general, the sensors responded to gases with different degrees of sensitivity. Among the sensors with higher surface areas, one provided noticeable enhancements in sensitivity towards gases when compared, for instance, to the sensitivity of the commercially based NiO sensor. The NiFe<sub>2</sub>O<sub>4</sub> sensor presented most promise as a gas sensor to ethanol and, to a greater or lesser degree, towards toluene gas. In general, sensors were poorly responsive to the carbon monoxide concentrations tested. This study is one of the first reports of using LJS-based powders for gas sensing applications and it highlights the suitability of the method to fabricate size- and shape-controlled nanomaterials for the detection of environmentally relevant gases.

**Keywords:** nickel oxide, nickel ferrite, nanoparticles, gas-sensing properties, detection, environmental monitoring

**DOI:** 10.3103/S1061386219030063

## 1. INTRODUCTION

In past decades, the fascinating and unique properties of nanostructured materials, together with their versatility for a wide range of applications have granted them steadily growing attention [1]. Among the various nanomaterials that have been studied, metal oxide semiconductors (MOS) have attracted increasing technological and industrial interest due to their properties, some of which include optical, magnetic, electrical, catalytic, and gas-sensing properties. These are associated with characteristics such as mechanical hardness, thermal stability or chemical passivity [2].

MOS gas sensors have been the subject of intense research, finding applicability in industrial process monitoring and control, and in environmental and indoor air quality measurements [3]. New technological advances have enabled a better control of the particle size, morphology, surface area, architecture, and

electrical properties of metal oxides [4] which, in turn, have resulted in great enhancements in sensor performance [5]. Industrial and domestic activities call for reliable and accurate gas detection systems, especially in relation to the associated concerns with environmental pollution that stem from them [3]. Solid-state metal oxide semiconductor gas sensors have been implemented for a range of commercial applications, but their greatest limitation is a result of their poor selectivity to gases when used in the bulk state [6]. Various methods, including temperature control and addition of surface additives or filtering layers, may be used to improve sensor selectivity [7]. One of the most effective ways in this direction goes through the nanoscale [8].

Simple transition metal oxides are very interesting examples of gas sensing materials. They can be prepared using a number of techniques, such as ultrasonic spray pyrolysis [9], liquid-control-precipitation [10],

chemical vapor deposition [11], electrodeposition [12], the sol–gel route [13], through the reduction of metallic salts followed by the oxidation of metallic species [14], pulsed laser ablation [15], and so on. Among such oxides, NiO nanoparticles exhibit multifunctional properties, suitable for a variety of applications including catalysis, electrochromic windows, battery cathodes and sensors [16, 17].

Nickel oxide (NiO) and ferrites such as  $\text{NiFe}_2\text{O}_4$  have recently surfaced as novel sensitive materials for the detection of both reducing and oxidizing gases that are important from environmental, safety, and medical perspectives [18–20].  $\text{NiFe}_2\text{O}_4$  is an inverse spinel in which the tetrahedral sites are occupied by  $\text{Fe}^{3+}$  ions and the octahedral sites, by  $\text{Fe}^{3+}$  and  $\text{Ni}^{2+}$  ions [21]. This material is widely used in electric and electronic devices as a magnetic material, and is also applied to the fields of catalysis and gas sensors due to its semiconducting properties [22]. Recently, much attention has been devoted to the controlled preparation of nanosized ferrites because the cation distribution and the resulting magnetic properties are found to be different when compared to those of the bulk counterparts [8, 23]. Meanwhile, this material has been confirmed as a good gas-sensing material [24], and its sensitivity is strongly correlated to its crystalline size [25].

Multiple methodologies have been developed to synthesise nanosized  $\text{NiFe}_2\text{O}_4$ , some of which include co-precipitation [26], the sol-gel method [27], and shock-wave [28], mechanical alloying, and pulsed-wire discharge methods [29]. However, there are no facile methods for the synthesis of nanocrystalline  $\text{NiFe}_2\text{O}_4$ , which is difficult or inconvenient to obtain through multistep syntheses methods. As such, a cost-effective and scalable technique able to synthesize and control the size and shape of Ni-based nanoparticles is needed [30].

The self-sustaining levitation-jet synthesis (LJS) method is an attractive technique that facilitates the simultaneous control of nanoparticle shapes and sizes [23, 31, 32]. A one-pot, fully regulated process does not require additional surfactants or capping agents. This, in turn, serves to minimize the number of precursors utilized and makes mass production of highly pure materials feasible [23].

In the present work, Ni/NiO and  $\text{NiFe}_2\text{O}_4$  nanopowders have been synthesized using an LJS method. Gas sensors have been developed from these materials and the morphology, phase composition, optical and magnetic properties of the materials has been evaluated. This is, to the best of our knowledge, the first time that an LJS method has been used to synthesize and compare the gas sensing properties of NiO nanoparticle materials – with a range of particle sizes, shapes and surface areas – to those of  $\text{NiFe}_2\text{O}_4$  nanoparticles. In addition to this, the performance of the LJS Ni-based nanoparticles has been compared to that of a NiO gas sensor fabricated using a commer-

cially sourced NiO powder. This particular sensing array has been tested in the presence of trace gas concentrations of ethanol, carbon monoxide, and toluene and the optimal operating temperature of these sensor systems has been explored and reported.

## 2. EXPERIMENTAL

### 2.1. Materials Synthesis

Nanoparticles were produced by using the modified levitation-jet method described in detail elsewhere [31, 33]. This technique may be described as self-sustaining oxidation method which is similar to the SHS process for production of simple and complex oxides. In this technique, a metal nickel droplet is suspended inside an appropriate quartz tube and heated up to melting and vaporization onset in electromagnetic field (0.44 MHz) generated by a counter-current inductor and supplied from an industrial HF generator. The levitated droplet is blown down by an adjustable stream of inert and reacting gas. Nanoparticle formation occurs at normal gas pressure. As an evaporated material, we used a wire of pure metal nickel (0.2 mm in diameter 99.9 at. % pure) which, by means of the appropriate feeding device, continuously feeds the liquid droplet at some constant rate. The vapor condensation rate is made equal to the rate of consumption of the metal wire, which can easily be regulated by varying the rotation speed of the feeding device rollers through a stepped motor. In order to synthesize the Ni/NiO nanoparticles, the necessary amount of gaseous oxygen/air is introduced into the main gas stream in the combined mode [31]. In regards to the synthesis of nickel ferrite, the second Fe wire (0.3 mm in diameter, 99.9 at. % pure) is simultaneously supplied to the levitated droplet. As-prepared particles are collected on a cloth filter and hereinafter removed into a container.

### 2.2. Materials Characterization

The crystal structure and phase compositions of the nanoparticles were determined by XRD (DRON-3M diffractometer,  $\text{Cu-K}_\alpha$  or  $\text{Fe-K}_\alpha$  radiation). The XRD phase analysis was performed using the Crystallographica Search-Match (v. 3.1.0.2) and PowderCell for Windows (ver. 2.4) programs and the Powder Diffraction File (PCPDFWIN ver. 2.02) database. Powder morphology was examined by TEM (JEM-1200EX II JEOL) and SEM (LEO 1450 Carl Zeiss). Electron micrographs were analyzed using AxioVision ver. 4.82 image processing program to determine the average particle size. The specific surface area of the loose nanoparticles was explored using a 4-point method that measures the physical adsorption of nitrogen onto the materials. BET analysis together with a SORBI-M META device was employed to do this.

**Table 1.** Synthetic conditions and some physicochemical characteristics of Ni-based nanoparticles under study

	Synthesis conditions	$\langle d \rangle$ , nm	Ni, at. %	$E_g$ , eV	$\sigma_s$ , emu/g	$S$ , m <sup>2</sup> /g
N1	He 500 L/h, Ni 1 g/h	23	83	2.22	42.3	29.84 ± 0.89
N2	He 1000 L/h, O <sub>2</sub> 200 L/h, Ni 1 g/h	8	~0	2.72	0.89	103.4 ± 1.06
N3	He 1000 L/h, O <sub>2</sub> 100 L/h, Ni 0.4 g/h	7	~0	3.28	1.0	117.2 ± 1.21
N4	NiO (TU 6-09-5095-83)	230	~0	3.18	1.81	3.77 ± 0.07
N5	NiO (Aldrich 6-67)	37 μm	~0	1.50	1.12	23.55 ± 1.69
N6	He 500 L/h, air 9 L/h, Ni 2 g/h, Fe 3.5 g/h	31	0	—	69.0	36.27 ± 3.73

The UV–VIS spectra of the nanoparticles (NPs) were recorded on a Lambda 950 (Perkin Elmer) using an integrated sphere detector. Fourier transform infrared (FT-IR) spectra were recorded in the solid phase using a Tensor 27 spectrometer with attenuated total reflectance (ATR) accessory (Bruker) in the frequency range of 400–4000 cm<sup>-1</sup>. Raman spectra were recorded at room temperature using an InVia Raman Renishaw and confocal microscope Leica DMLM apparatus with an air-cooled charge-coupled device coupled with He–Cd and Ar lasers emitting at 325 nm and 514 nm, respectively.

XPS spectra were collected using a Thermo Scientific X-ray Photoelectron Spectrometer. It utilizes a monochromated Al-K<sub>α</sub> (1486.6 eV) source running at the power of 72 W with a pass energy of 50 eV, which was used for high resolution region scans, and 200 eV, which was used for survey scans. Finally, for the charge corrections a one-point scale with the C 1s peak shifted to 285.0 eV was used. The magnetic properties of the NPs were measured by means of a Quantum Design VSM/SQUID magnetometer which was calibrated using a Dy<sub>2</sub>O<sub>3</sub> standard with a relative accuracy of 10<sup>-6</sup> emu at room temperature. During the experiments, the magnetic field was ramped from zero to 70 kOe at 300 K.

### 2.3. MOS Sensor Fabrication

The as-prepared nanoparticles were mixed into an ink using a previously reported method [34]. The inks were screen printed directly onto gold interdigitated electrodes on 3 × 3 mm alumina chips. They were then treated in furnace at 600°C for 1 h to burn the organic phase of the ink off, and ensure adherence of the powders to the sensor substrates [35, 36]. Following heat treatment, 50-μm platinum wire was spot-welded onto the gold contacts on the fired sensor chips and, in turn, spot-welded on stainless steel pins in molded polyphenylene sulfide housings that enabled the sensor's suspension in the center of the housing. Gas sensing experiments were performed in an in-house gas-sensing rig [35] designed to maintain up to twelve sensors at a constant operating temperature, which may be modified in the range of 300 to 500°C, using a heater driver circuit connected to each of the sensors'

heater track. The sensors were exposed to a range of BOC gases (ethanol, toluene, and carbon monoxide) at environmentally relevant trace gas concentrations [3]. The gas concentrations investigated here are significant in air-quality and environmental monitoring and also in medical and security fields.

## 3. RESULTS AND DISCUSSION

### 3.1. Powder X-Ray Diffraction (PXRD)

XRD patterns in Fig. 1 show the reflections of pure rhombohedral NiO (JCPDS card no. 44-1159) with lattice parameters:  $a = 2.955 \text{ \AA}$  and  $c = 7.228 \text{ \AA}$  for samples N1–N6 (see Table 1 for the nomenclature and relevant parameters of each sample). For sample N1, cubic Ni reflections (JCPDS card no. 04-0850) with  $a = 3.524 \text{ \AA}$  were also identified as the main phase. No other phases or impurities were detected with XRD. Figure 1 also displays the diffraction pattern of the N6 nickel ferrite sample (JCPDS card no. 44-1485), showing a single-phase cubic spinel structure, with lattice parameter  $a = 8.339 \text{ \AA}$ . These lattice parameters were identical to those reported in the literature, within experimental error [37].

### 3.2. TEM and SEM

Electron microscope imaging of the Ni-based nanoparticles (Fig. 2) indicated a cubic morphology with average particle sizes that were less than 100 nm in all the Ni/NiO samples. An exception was observed in the commercially based N4 and N5 materials which, in turn, appeared more oval in shape and interconnected. The NiFe<sub>2</sub>O<sub>4</sub> sample (Fig. 2f, sample N6) displayed a significantly different morphology. Its particle shape was predominantly hexagonal. The specific surface area of the materials ( $S$ ) proved to be comparable to the mean particle size ( $\langle d \rangle$ ) calculations carried out using relevant micrographic analysis.

### 3.3. Raman Spectroscopy

Raman spectroscopy is very sensitive to the microstructure of nanocrystalline materials. It has also been used here to clarify the structure of the Ni-based nanoparticles. The Raman spectrum of pure NiO car-

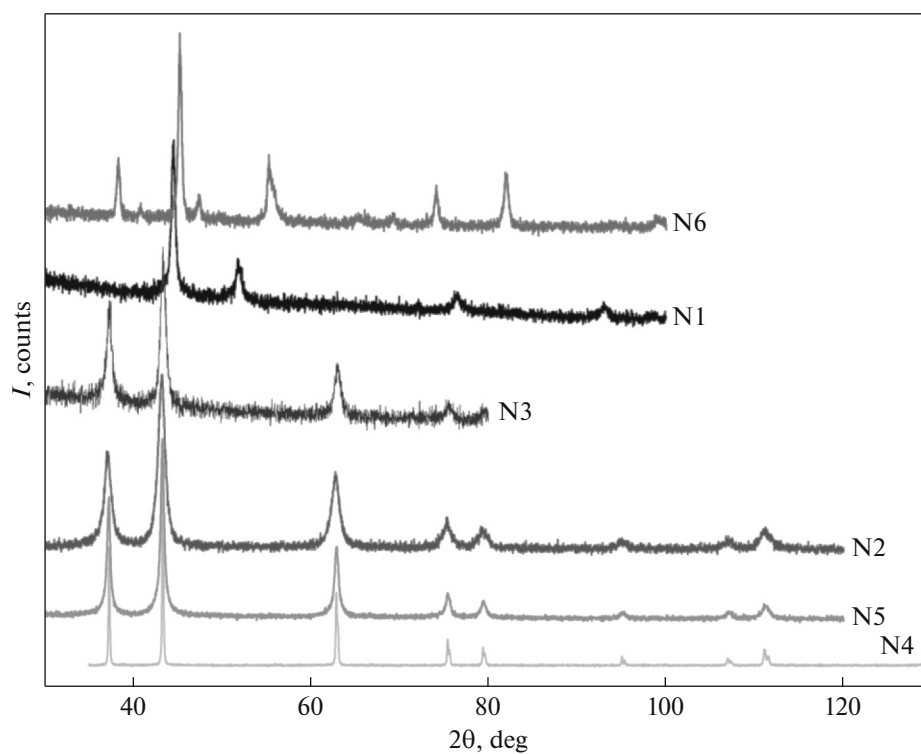


**Fig. 1.** Diffraction patterns of Ni-based nanoparticles under study. The sample nomenclature corresponds to that presented in Table 1.

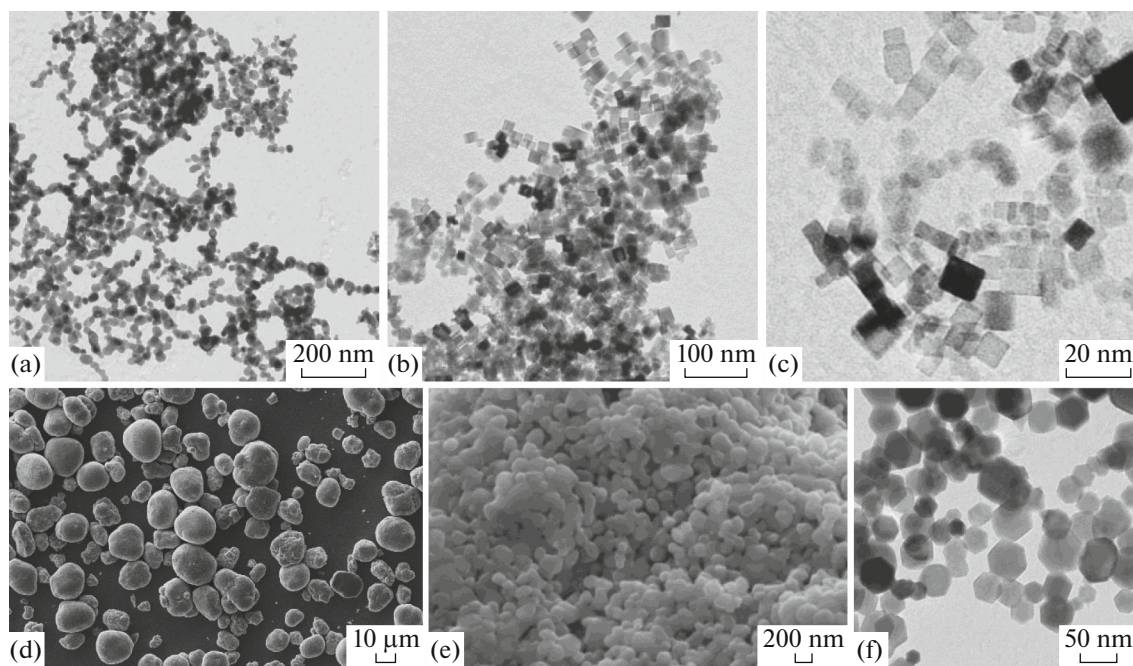


**Fig. 2.** Electron images of Ni-based nanoparticles: (a) N1, (b) N2, (c) N3, (d) N4, (e) N5, and (f) N6 (for sample nomenclature see Table 1).

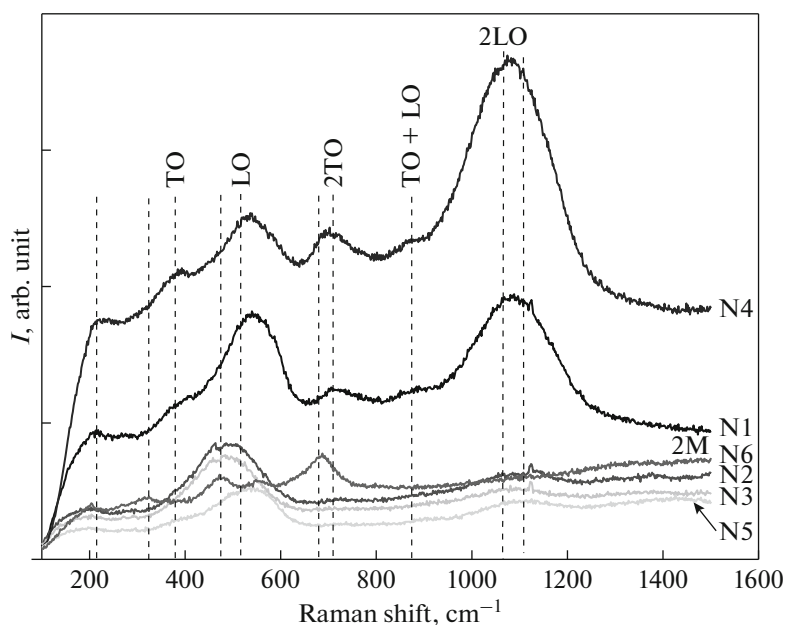


Fig. 3. Raman spectra of Ni-based nanoparticles. Sample nomenclature is the same as in Table 1.

ried out at room temperature consists of several bands: five vibrational bands of one phonon (1P) TO (at 400–440  $\text{cm}^{-1}$ ) and LO (at 560  $\text{cm}^{-1}$ ) modes, two-phonon (2P) 2TO modes (at 740  $\text{cm}^{-1}$ ), TO + LO (at 925  $\text{cm}^{-1}$ ), and 2LO (at 1100  $\text{cm}^{-1}$ ) modes, and two-magnon (2M) bands at 1500  $\text{cm}^{-1}$  [38]. Most of our NiO samples (Fig. 3) show obvious Raman bands located at approximately 380, 520, 710, 880, and 1080  $\text{cm}^{-1}$ . These Raman shifts are consistent with those of nanosized NiO [39]. The strong band seen at 520  $\text{cm}^{-1}$  belongs to the longitudinal (LO) one phonon (1P) mode and corresponds to the 1080  $\text{cm}^{-1}$ , which is due to two phonon (2P) modes of the 2LO peak. It was observed that the intensities of the two Raman bands increased with increasing nanoparticle size. There was no magnon band in the Raman spectrum, which is normally observed at 1500  $\text{cm}^{-1}$ . The absence of a magnon band in the data suggests that a reduction of the spin correlation is the result of a phase transition from antiferromagnetic to paramagnetic, when the particle size is reduced to the nano level [40]. From this it can be concluded that a reduction in nanoparticle sizes of NiO samples leads to a transformation into a paramagnetic phase. However, the ferrite sample (N6) revealed 2M bands, whereas other bands were less pronounced.

### 3.4. FTIR Spectroscopy

Figure 4 shows some of the results attained when investigating the materials with FTIR spectroscopy. There were peaks in the region ranging from 400 to 850  $\text{cm}^{-1}$ , due to the oxide structure. There were two

broad peaks at 3400 and 1650  $\text{cm}^{-1}$ , which corresponded to the O–H stretching vibration of surface-adsorbed water and H–O–H bending vibration mode of the hydroxyl groups, respectively, due to the adsorption of moisture from the air [41].

### 3.5. UV–VIS Spectroscopy

In the UV–VIS diffuse reflectance spectra for samples N2–N5 (Fig. 5), the long tails of the reflectance at long wavelengths were attributed to the scattered radiation of nickel oxide clusters of nanoparticles. All the spectra were analyzed using the Kubelka–Munk function  $F(R_a)$  [42] which is related to the diffuse reflectance as follows:

$$F = (1 - R_a)^2 / 2R_a,$$

where  $R_a$  is the absolute reflectance and  $F$  is an equivalent to the absorption coefficient. A better approach is to determine the indirect band gap,  $E_g$ , of the nanoparticles, which was estimated by plotting  $(FE)^{0.5}$  values as a function of photon energy  $E$  (dashed lines in Fig. 5), according to [43]. The linear portion of the curves was extrapolated to zero in order to determine the band gap value [44]. Analysis of Fig. 5 revealed that, for the large-sized nanoparticles, large variations in reflectance with wavelength were observed, when compared to the small-sized nanoparticles. No linear relation with the Tauc plot for  $(FE)^2$  [45] was found, suggesting that Ni-based oxide nanoparticles are semiconducting, with indirect transition to the band gap energy, which is in stark contrast with previously reported data [46].

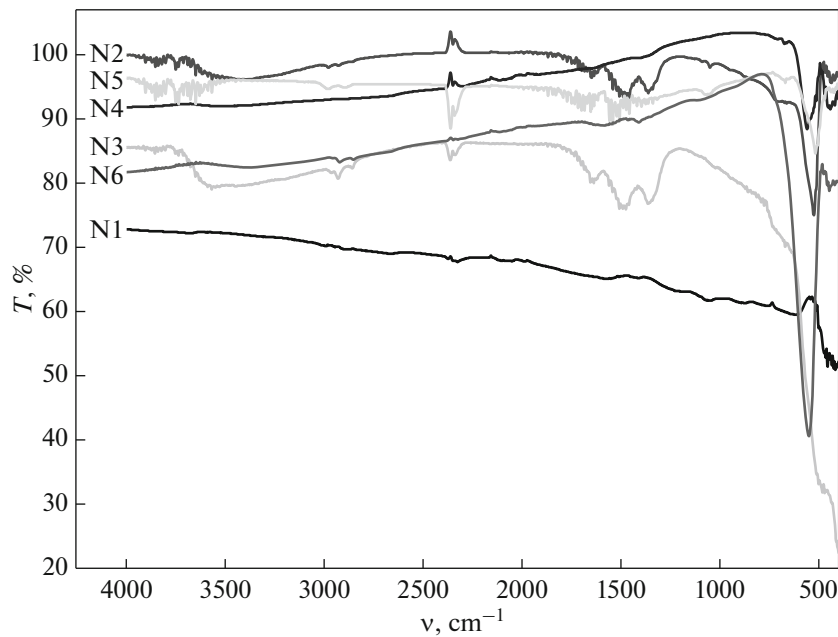


Fig. 4. FTIR spectra of Ni-based nanoparticles.

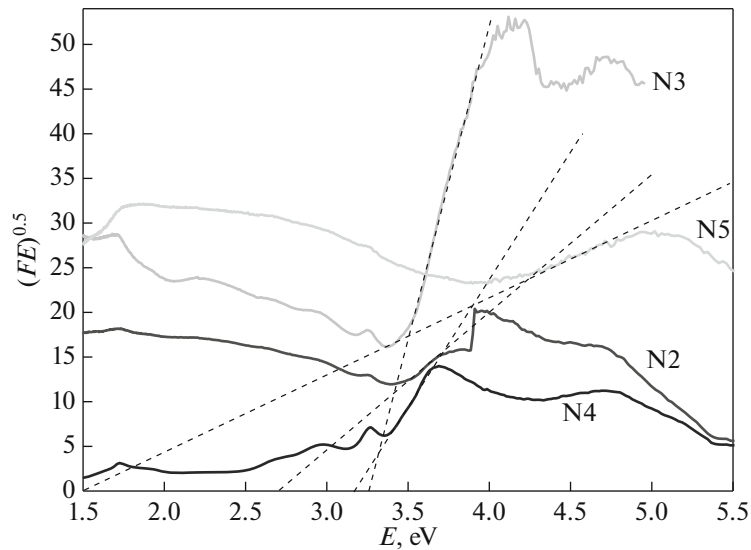


Fig. 5. Reflectance spectra for samples N2–N5 plotted using the Kubelka–Munk function and evaluation of band gaps  $E_g$ .

### 3.6. XPS Spectroscopy

The surface composition and chemical states of the materials were determined by means of XPS spectroscopy, according to the characteristic binding energies of the different elements on the materials' surfaces. The varied physical properties of Ni-based nanoparticles are due to the dominant contributions from their defect structure; particularly, the cation ( $\text{Ni}^{2+}$ ) and anion ( $\text{O}^{2-}$ ) vacancies, which are the major source of defects in NiO [47]. The presence of each  $\text{Ni}^{2+}$  vacancy in the lattice leads to the transformation of

two adjacent  $\text{Ni}^{2+}$  ions into  $\text{Ni}^{3+}$  ions to acquire charge neutrality, thereby inducing a lattice distortion. Each  $\text{Ni}^{2+}$  vacancy along with two  $\text{Ni}^{3+}$  ions in opposite nearest neighbor positions constitute a bound quadrupole. If a  $2p$  electron from the nearby  $\text{O}_2^-$  ion is transferred to a  $\text{Ni}^{3+}$  ion of the quadrupole, then a hole will be induced in the  $2p$  band of  $\text{O}^{2-}$  [48]. The presence of  $\text{Ni}^{3+}$  ions in the samples was established by XPS measurements, the results of which are shown in Fig. 6. The two sharp peaks at 854.0 eV and 872.7 eV in the Ni  $2p$  spectrum correspond to Ni  $2p_{3/2}$  and Ni  $2p_{1/2}$  (Fig. 6a).



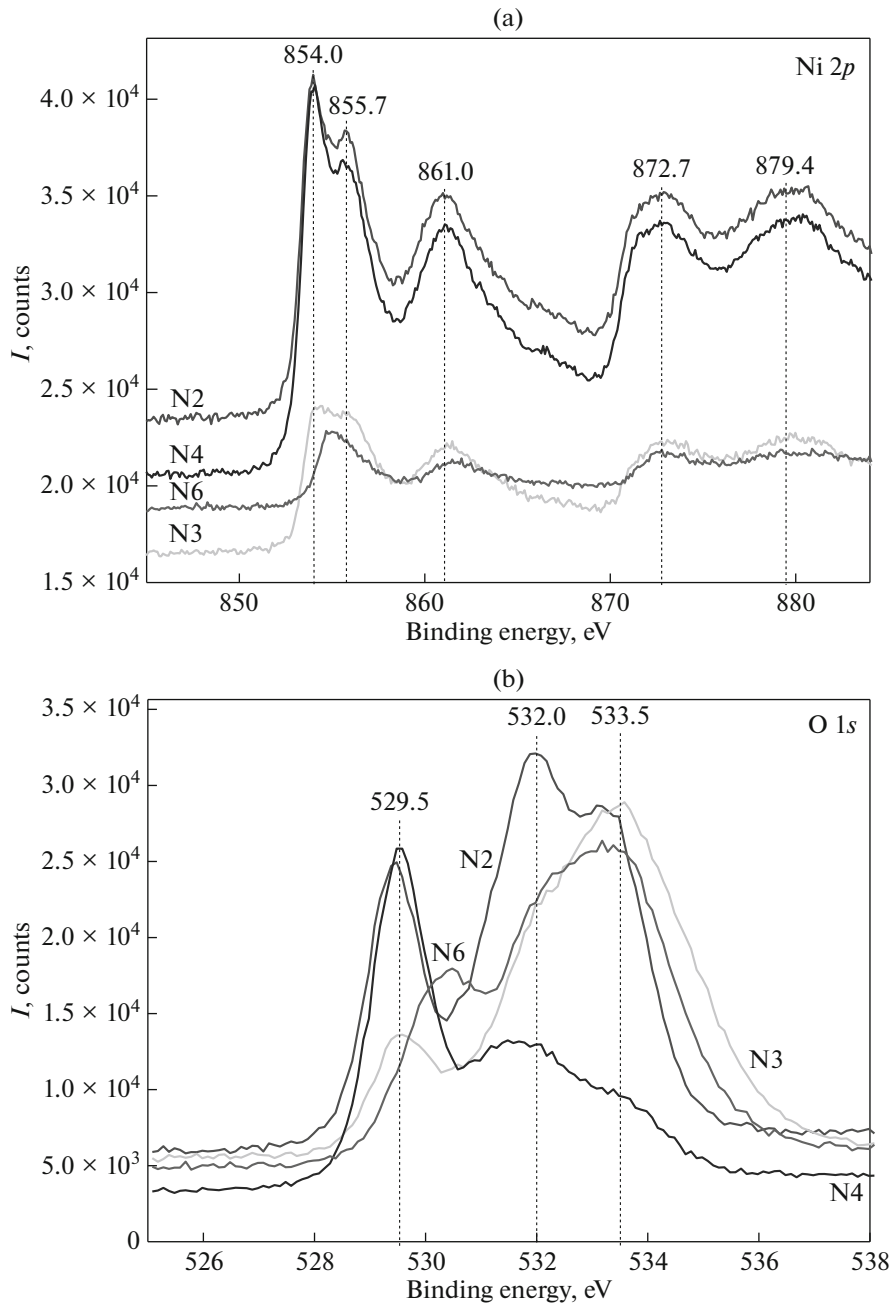
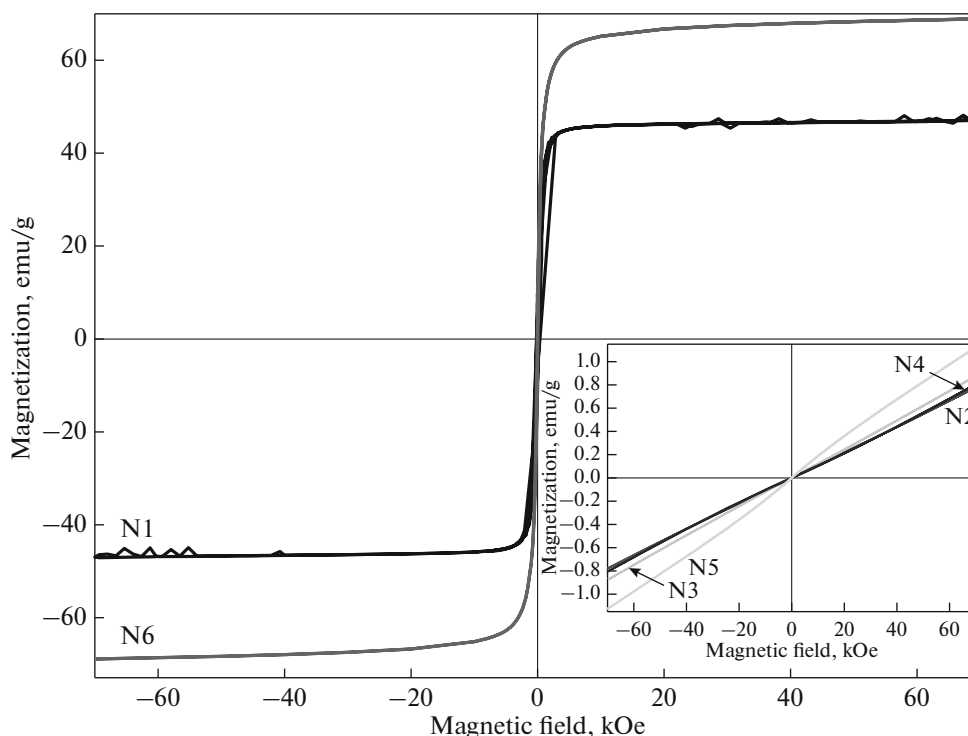


Fig. 6. XPS spectra of (a) Ni 2p and (b) O 1s for Ni-based nanoparticles.

Satellite peaks at 879.4 and 861.0 eV are present as a result of the shake-up processes [49]. In regards to the O 1s spectra of the N2 sample (Fig. 6b), the peaks that appear at about 529.5 and 532.0 eV correspond to the  $O^{2-}$  ions bonded to  $Ni^{2+}$  and  $Ni^{3+}$ , respectively. For the N3 sample, corresponding peaks were obtained at 529.6 and 533.5 eV. After comparison of the peak intensities of the two samples, it was clear that the presence of  $Ni^{3+}$  in the last sample had diminished considerably [47]. Hence, it may be concluded that the presence of uncompensated  $Ni^{2+}$  vacancies are less

and, as such, the concentration of  $O^{2-}$  vacancies is comparatively more abundant in the last sample and in the ferrite material as well (sample N6). Another plausible interpretation for the peak observed near 856 eV can be found in [50]. This spectrum cannot be satisfactorily fitted with the unaltered  $Ni^{2+}$  multiplets (as it was the case of sample N6) or with the FWHM variation alone. A satisfactory fit can only be achieved by allowing variation in the BE positions of the multiplet contributions to the main peak.



**Fig. 7.** Hysteresis loops for the samples prepared under non-oxidizing conditions (N1, N6) and those prepared under oxidizing conditions (N2–N5, inset).

There is also a broad peak associated with other intrinsic losses at a higher binding energy than that of the main peak multiplets. In all of the above-mentioned cases, this contribution is necessary in order to model the valley between the main peak and the satellite structures and is consistent with the inter-band losses [50]. In the Fe  $2p$  spectra (sample N6), the peak shape was very broad, which may indicate several Fe-containing species e.g. Fe-OH. Fitting suggests that the chemical state of the iron was largely Fe<sup>3+</sup>. However, the presence of some Fe<sup>0</sup> and Fe<sup>2+</sup> cannot be ruled out.

### 3.7. Magnetic Measurements

Figure 7 presents the magnetic hysteresis loops measured at room temperature for the samples prepared under non-oxidizing conditions (N1, N6) and those prepared under oxidizing conditions (N2–N5).

Magnetic characterization revealed that samples N1 and N6 showed ferromagnetic-like hysteresis loops (Fig. 7). Saturation magnetization values at 300 K increased with the Ni content in sample N1, approaching that of bulk Ni at 300 K (55 emu/g). The inset in Fig. 7 presents a set of hysteresis loops for selected samples, previously listed in Table 1. All loops showed almost superparamagnetic behavior with very little hysteresis and with coercivity lower than 100 Oe. Specific magnetization  $\sigma_s$  showed a nearly linear

dependence at high fields and reached maximum values under 1 emu/g at 70 kOe [51].

## 4. GAS SENSING

The gas-sensing properties of NiO nanoparticles and of NiFe<sub>2</sub>O<sub>4</sub> fabricated with an LJS method were investigated in this study. These were, in turn, compared to the sensing properties of a NiO sensor that was fabricated using commercial powders. As reported previously, the surface area, shape and size of the LJS nanoparticles differed across the range of test sensors. It was therefore noteworthy to investigate whether the microstructure and morphology of the materials had an effect on the sensing performance of the sensors.

Bearing in mind that MOS-based sensors often see a so-called ‘sensitivity maximum’ when they are exposed to a test gas and heated to temperatures that typically fall in the range of 200–500°C [52], it was key to understand how the newly-fabricated sensors behaved under different experimental conditions and how these might improve or worsen the sensitivity and/or selectivity of the devices towards test gases. Furthermore, it was especially noteworthy to investigate how the NiO gas sensor fabricated with a commercial powder performed, in relation to those fabricated using the LJS method. The comparison extended to studying the effects that the incorporation of iron—to form NiFe<sub>2</sub>O<sub>4</sub>—had on the functionaliza-



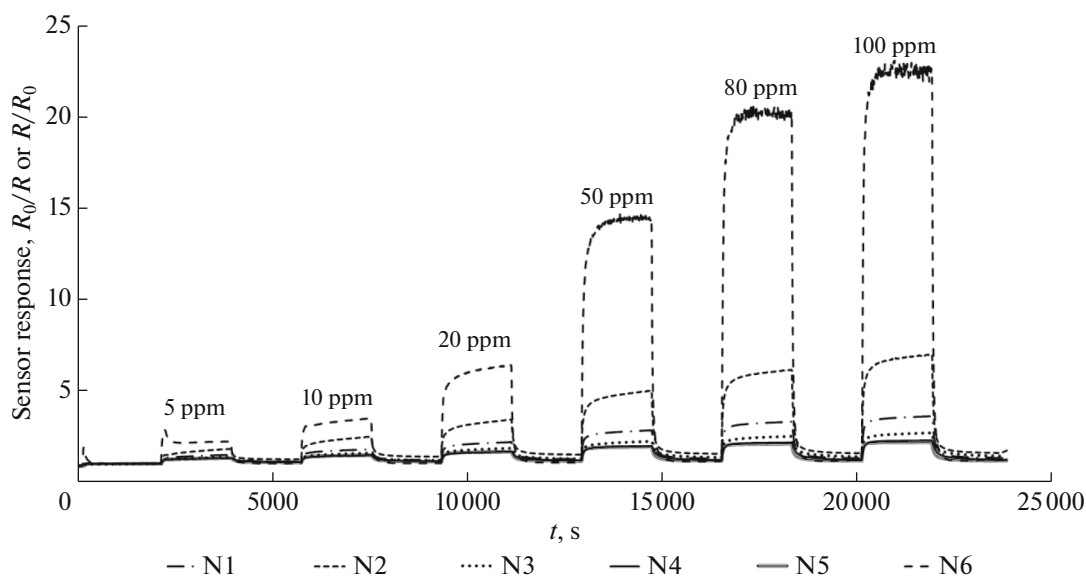


**Fig. 8.** Gas responses of sensors to varying concentrations of ethanol (5, 10, 20, 80, and 100 ppm) at 300°C. Note that the ferrite sensor (N6) displayed  $n$ -type behavior so that its response was therefore calculated as  $R_0/R$ .

tion of the sensors at the time of detecting the following test gases: ethanol, toluene, and carbon monoxide.

As extensively discussed in the field, it is often desired to have a device that will display complete specificity towards a gas, particularly when the analyte is in the presence of other interfering gases [53]. However, because this is a complex task, other ways of achieving selectivity are generally sought. For instance, an array of different sensors displaying partial specificity towards gases may be used, [54] and/or the operating temperatures of the sensors may be modulated [55] such that a fingerprint is essentially generated upon sensor exposure to each gas. Furthermore, data mining tools based on supervised or unsupervised machine learning methods can then assist in discriminating across test analytes [35, 56].

NiO is a  $p$ -type semiconductor material and its suitability as a gas sensor has already been established in the literature. The sensing properties of  $\text{NiFe}_2\text{O}_4$  have also been reported in other studies. It is commonly a  $p$ -type semiconductor, its behavior stemming from the hole ( $h^+$ ) hopping between  $\text{Ni}^{2+}$  and  $\text{Ni}^{3+}$  in octahedral sites [57]:  $\text{Ni}^{2+} + h^+ \leftrightarrow \text{Ni}^{3+}$ .

In this study, the commercially-based NiO sensor and those fabricated with NiO nanoparticles displayed  $p$ -type conductivity, as originally expected. Conversely, the nickel ferrite sensor displayed  $n$ -type conductivity. Results are presented and discussed in more detail below.

#### 4.1. Sensor Exposure to Ethanol

The sensors were most responsive to ethanol gas at 300°C. Figure 8 shows the sensor responses and peak

shape patterns attained when exposing the sensors to different concentrations of ethanol at 300°C. In the latter figure, it can be seen that the nickel ferrite sensor was consistently the most responsive one and it displayed flat peak shape characteristics that are commonly sought in practical settings. More specifically, the sensor saturated and reached steady state, particularly when exposed to 50, 80, and 100 ppm of the gas. As expected, at lower operating temperatures the sensors' response times were longer and ranged between 99 and 299 s, which could be undesirable in practical applications. These results are in line with what other studies investigating NiO-based nanoparticles have reported [58]. With lower ethanol concentrations, the sensors took even longer times to respond. In regards to the recovery times of the sensors, most failed to fully recover in the allocated recovery time. Nevertheless, the nickel ferrite sensor fully recovered in just over a minute. It must be noted that the shark-fin shape that is observed in some sensors is indicative of an unsaturated surface, and suggests that the dynamic range of the sensors is greater than that investigated here.

It is interesting to see that the greater surface area of some sensors, namely N2 and N3 ( $S = 103$  and  $117 \text{ m}^2/\text{g}$ , respectively), did not lead to the expected improvements in sensor response that were observed with sensor N6 (nickel ferrite) which, in turn, had a surface area of  $36.2 \text{ m}^2/\text{g}$  and larger particle size of  $\sim 31 \text{ nm}$ , in relation to  $8 \text{ nm}$  and  $7 \text{ nm}$  of samples N2 and N3, respectively. The N4 and N5 (commercial NiO powders) sensors responded to ethanol gas comparatively. This was in spite of the larger particle size of the N5 material and their very different particle morphology (cf. Figs. 2d, 2e). It is thought that the enhanced responsiveness to ethanol seen in sensor N2 was

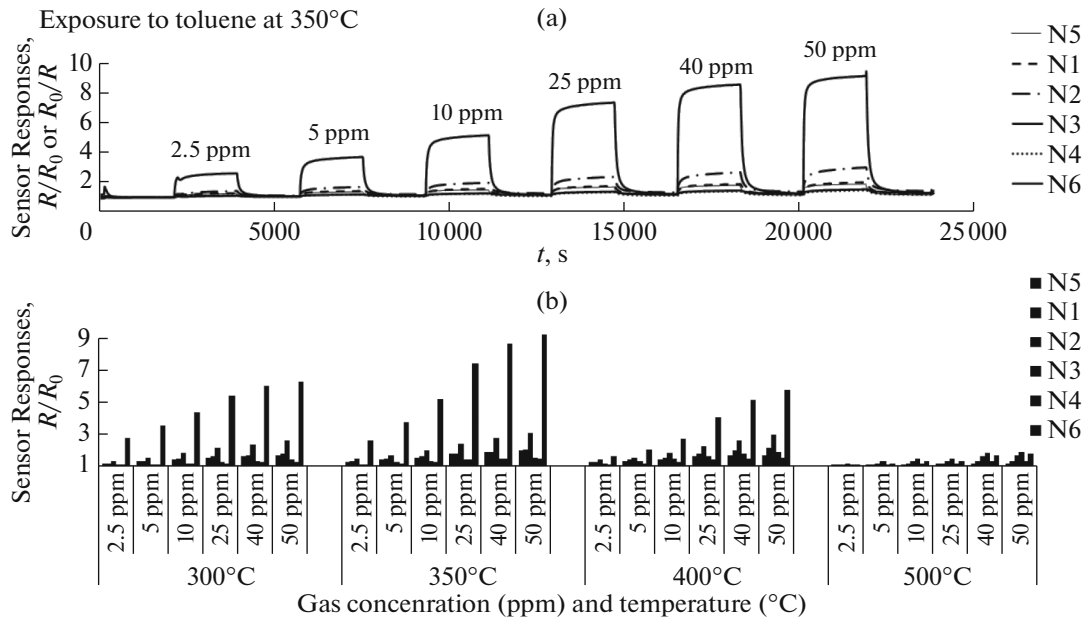


**Fig. 9.** (a) Gas responses of sensors to varying concentrations of toluene (2.5, 5, 10, 25, 40, 50 ppm) at 350°C and (b) gas responses to toluene concentrations at different temperatures. The histograms in Fig. b go (from left to right) in the order: N5, N1, N2, N3, N4, N6. Note that N6 behaved as an  $n$ -type semiconductor so that its response was thus calculated as  $R_0/R$ .

because of its higher surface area and higher concentration of surface-reactive sites available for gas interaction. It is thought that a more open and porous sensing material microstructure can result in amplification of material's conductivity [7]. It must be noted, however, that despite the similarities in surface area and particle size of sensors N2 and N3, the responsiveness of the latter to ethanol was more conservative. It is possible that the microstructure of this sensor was affected differently during the sensor's heat treatment process, leading to the observed lower sensor responses. Sensing materials with different particle shapes can provide adsorption sites for gases with different energies [20]. As such, it is interesting to see that sensors N1 and N2, for instance, displayed very different particle sizes and shapes, yet they were both responsive to ethanol at 300°C, rendering them as promising gas sensor candidates, particularly when supplied with ethanol concentrations that were equal to or exceeded 50 ppm. The relatively high sensitivity of the  $\text{NiFe}_2\text{O}_4$  sensor may be attributed to the large number of step and kink sites, which may allow the preferential adsorption and ionization of oxygen at the materials interface.

Other studies have also investigated Ni-based materials for ethanol detection. For instance,  $\text{NiO}/\text{NiFe}_2\text{O}_4$  composites were prepared [19] to determine the sensing performance of the new sensors at room temperature. The sensors showed good sensitivity to gases such as ethanol, acetone, THF, and methanol. However, the concentrations tested were well in excess of concentrations sought in environmental-

monitoring practices. In [59], a NiO nanoplate sensor was modified by mixture with a ZnO material to obtain selectivity towards 500 ppm ethanol gas ( $R/R_0 \approx 35$ , in relation to  $R/R_0 < 2.5$  that they obtained with sensor exposure to gases such as  $\text{CO}$ ,  $\text{H}_2$ ,  $\text{H}_2\text{S}$ ).

#### 4.2. Sensor Exposure to Toluene

Sensors were also exposed to toluene gas; the results are presented in Fig. 9. As observed in the figure, the sensors were most responsive to toluene at 350°C.

With the exception of the N6 (nickel ferrite) sensor, which was the most responsive to the gas, the other LJS-based nanoparticle sensors and the commercially-based NiO sensor were not particularly sensitive to toluene. It is noteworthy that the N6 sensor was responsive to trace concentrations of toluene i.e. 2.5–50 ppm and, for this reason, lower concentrations would be worth testing in future. The sensor responded linearly when supplied with toluene concentrations ranging between 2.5–25 ppm. The response vs. concentration curve appeared to saturate when supplied with higher concentrations of toluene, suggesting a limited dynamic range of the sensor towards this gas. At 350°C, the nickel ferrite sensor provided a  $\sim 4.8$  enhancement in sensor response over the commercially-sourced NiO sensor (N5), when supplied with 50 ppm of gas.

Sensor N2 also provided promising outcomes for toluene detection, albeit the rather conservative response attained, in relation to that of sensor N6.

Sensors N1, N3, N4, and N5 responded very similarly to toluene, despite the important differences in surface area, particle size, morphology, and synthesis procedure.

NiO nanostructures have been proposed in the literature as a great material for the detection of toluene, particularly when doped with chromium [60]. The Cr-doped nanostructures were found to be selective towards the gas, in relation to the responses that were attained when exposing the sensor to molecules with similar molecular structures e.g. benzene and xylene. Other studies have utilized  $\alpha$ -Fe<sub>2</sub>O<sub>3</sub>/NiO composites with a hollow nanostructure for the selective detection of the gas [61]. The response magnitude of the composite sensor they investigated was comparable to that of the NiFe<sub>2</sub>O<sub>4</sub> sensor presented here when exposed to concentrations of 5 ppm and 10 ppm.

Other studies that fabricated NiFe<sub>2</sub>O<sub>4</sub> using an inverse titrating chemical co-precipitation technique reported lower sensing responses to higher concentrations of toluene than reported here [62]. However, their sensor displayed selectivity towards toluene, in relation to other gases such as methane, ethanol, carbon monoxide, and ammonia. NiO/Fe<sub>2</sub>O<sub>3</sub> composites have been reported to show great sensitivity towards toluene, in relation to other gases such as ethanol, propanol, acetone, and THF [19]. Similar results were found when co-doping NiO with Li and Ti, where the sensor provided a clear advantage for the detection of toluene and not towards other gases [58].

#### 4.3. Sensor Exposure to Carbon Monoxide

The sensors were also exposed to carbon monoxide, at concentrations that ranged between 50–500 ppm and also at various temperatures (300–500°C). However, the sensors were almost unresponsive to these test concentrations and this was true across the temperatures investigated. Similar results were reported by [62, 63] upon exposure to CO concentrations <500 ppm with a NiFe<sub>2</sub>O<sub>4</sub> sensor. The sensor responses increased slightly when supplied with CO concentrations that exceeded 1000 ppm [62] but their sensor was unable to differentiate between CO and CH<sub>4</sub> gases.

## 5. SUMMARY AND OUTLOOK

Although a few studies have, indeed, evaluated the gas sensing properties of NiFe<sub>2</sub>O<sub>4</sub>, [62, 64, 65], a very limited number of gases have been previously evaluated and poor sensitivity and selectivity of the sensors has typically been reported [4, 66]. Generally speaking, the nickel ferrite sensors are commonly found to be selective towards a particular gas, but the gas concentrations investigated have commonly been very high [4, 67, 68], and far in excess of what can reasonably be expected in real-world investigations of environmental pollutants [3]. Conversely, the nickel ferrite

gas sensor prepared here provided excellent sensor performance when exposed to trace gas concentrations and it responded very differently to all the gases that were investigated which, in turn, makes it a good candidate as a selective sensor in future investigations.

The LJS method employed here to synthesize nanoparticle materials offers very attractive advantages over other synthesis methods, such as enabling particle size and shape control and not requiring additional surfactants or capping agents which, consequently, reduces the number of precursors needed for fabrication and facilitates large-scale production of highly pure materials.

It is worth noting that the sensing performance of the LJS nickel ferrite sensor was far better than the other LJS NiO nanoparticle-based sensors prepared in this study and also in relation to that of the NiO sensor prepared using a commercial powder. Sensor N1 and N2 also showed promise for future gas sensing investigations. Although N1 and N2 were both responsive to gases such as ethanol, the former displayed particle morphologies that were oval in shape, whereas the latter had a higher surface area and particle morphologies that were square in appearance. Conversely, it was interesting to see that although sensors N2 and N3 had similar microstructures and particle morphologies, they responded rather differently to the test gases. This may be the result of the different synthesis conditions used to fabricate the materials and/or the result of the materials sintering differently when undergoing heat treatment during the sensor fabrication steps. This may have affected the microstructure of the sensing materials such that the access of the gases through the sensing system was somewhat limited in the N3 sensor microstructure. Further work ought to be carried out in future to investigate this in depth. The sensors were typically more responsive to gases at 350°C, which is in line with what other groups investigating Ni-based gas sensors have reported in the literature [62].

It has been shown here that modifying the synthesis conditions of the LJS method could lead to the different particle properties that worked in favor of gas detection. When the LJS method synthesized particles that were comparable to those of the commercially sourced NiO powder, the gas sensing results were very similar among sensors. This study illustrates the value of LJS as an excellent and straightforward means of fabricating nanoparticle materials but, also, as a means of fabricating materials that may be used for the purposes of trace gas detection and with improved sensing performance over commercially-sourced powder materials.

## 6. CONCLUSIONS

A self-sustaining levitation-jet synthesis (LJS) was employed to synthesize a range of nickel-based metal oxide nanoparticles in order to assess their feasibility

as gas sensing materials. The properties of the LJS-based sensors were compared to those of a NiO sensor fabricated with a commercially sourced material. The sensing performance of the LJS-fabricated sensors was typically enhanced in relation to that of the sensor fabricated with the commercial NiO powder. Very interestingly, NiFe<sub>2</sub>O<sub>4</sub> gas sensor provided the most responsive sensor outputs to the gases of interest, despite having other sensors in the array that had much-increased surface areas. Furthermore, this sensor alone responded to the gases with different degrees of sensitivity, highlighting its potential as a selective sensor if used as part of a gas sensor array. As a technique, LJS shows great promise for the production of oxide and complex oxide materials and it has provided excellent control of the nanoparticle sizes, morphology, and phase compositions. This, in turn, has led to the performance of the gas sensors investigated here to be very attractive for future environmental and air-quality applications.

#### ACKNOWLEDGMENTS

We would like to acknowledge Dr. Steve Firth and Dr. Sanjayan Sathasivam for their help with the analyses carried out in this study.

#### REFERENCES

- Hu, S. and Wang, X., Ultrathin nanostructures: Smaller size with new phenomena, *Chem. Soc. Rev.*, 2013, vol. 42, no. 12, pp. 5577–5594. <https://doi.org/10.1039/C3CS00006K>
- Wang, X., Zhuang, J., Peng, Q., and Li, Y., A general strategy for nanocrystal synthesis, *Nature*, 2005, vol. 437, pp. 121–124. <https://doi.org/10.1038/nature03968>
- Fine, G.F., Cavanagh, L.M., Afonja, A., and Binions, R., Metal oxide semiconductor gas sensors in environmental monitoring, *Sensors*, 2010, vol. 10, no. 6, pp. 5469–5502. <https://doi.org/10.3390/s100605469>
- Darshane, S.L., Suryavanshi, S.S., and Mulla I.S., Nanostructured nickel ferrite: A liquid petroleum gas sensor, *Ceram. Int.*, 2009, vol. 35, no. 5, pp. 1793–1797. <https://doi.org/10.1016/j.ceramint.2008.10.013>
- Afzal, A., Cioffi, N., Sabbatini, L., and Torsi, L., NO<sub>x</sub> sensors based on semiconducting metal oxide nanostructures: Progress and perspectives, *Sens. Actuators B: Chem.*, 2012, vols. 171–172, pp. 25–42. <https://doi.org/10.1016/j.snb.2012.05.026>
- Williams, D.E., Semiconducting oxides as gas-sensitive resistors, *Sens. Actuators B: Chem.*, 1999, vol. 57, nos. 1–2, pp. 1–16. [https://doi.org/10.1016/S0925-4005\(99\)00133-1](https://doi.org/10.1016/S0925-4005(99)00133-1)
- Binions, R., Afonja, A., Dungey, S., Lewis, D.E., Parkin, I.P., and Williams, D.E., Discrimination effects in zeolite modified metal oxide semiconductor gas sensors, *IEEE Sens. J.*, 2011, vol. 11, no. 5, pp. 1145–1151. <https://doi.org/10.1109/JSEN.2010.2084079>
- Lee, P.Y., Ishizaka, K., Suematsu, H., Jiang W., and Yatsui, K., Magnetic and gas sensing property of nano-sized NiFe<sub>2</sub>O<sub>4</sub> powders synthesized by pulsed wire discharge, *J. Nanopart. Res.*, 2006, vol. 8, no. 1, pp. 29–35. <https://doi.org/10.1007/s11051-005-5427-z>
- Oh, S.W., Bang, H.J., Bae, Y.C., and Sun, Y.-K., Effect of calcination temperature on morphology, crystallinity and electrochemical properties of nanocrystalline metal oxides (Co<sub>3</sub>O<sub>4</sub>, CuO, and NiO) prepared via ultrasonic spray pyrolysis, *J. Power Sources*, 2007, vol. 173, no. 1, pp. 502–509. <https://doi.org/10.1016/j.jpowsour.2007.04.087>
- Deng, X. and Chen Z., Preparation of nano-NiO by ammonia precipitation and reaction in solution and competitive balance, *Mater. Lett.*, 2004, vol. 58, nos. 3–4, pp. 276–280. [https://doi.org/10.1016/S0167-577X\(03\)00469-5](https://doi.org/10.1016/S0167-577X(03)00469-5)
- Ahmad, U., Kim, B.-K., Kim, J.-J., and Hahn, Y.-B., Optical and electrical properties of ZnO nanowires grown on aluminium foil by non-catalytic thermal evaporation, *Nanotechnology*, 2007, vol. 18, no. 17, 175606. <https://doi.org/10.1088/0957-4484/18/17/175606>
- da Fonseca, C.N.P., de Paoli, M.-A., and Gorenstein, A., The electrochromic effect in cobalt oxide thin films, *Adv. Mater.*, 1991, vol. 3, no. 11, pp. 553–555. <https://doi.org/10.1002/adma.19910031107>
- Hayat, K., Gondal, M.A., Khaled, M.M., and Ahmed, S., Effect of operational key parameters on photocatalytic degradation of phenol using nano nickel oxide synthesized by sol–gel method, *J. Mol. Cat. A*, 2011, vol. 336, nos. 1–2, pp. 64–71. <https://doi.org/10.1016/j.molcata.2010.12.011>
- Illy-Cherrey, S., Tillement, O., Dubois, J.M., Massicot, M., Fort, Y., Ghanbaja, J., and Bégin-Colin, S., Synthesis and characterization of nanosized nickel(II), copper(I) and zinc(II) oxide nanoparticles, *Mater. Sci. Eng. A*, 2002, vol. 338, nos. 1–2, pp. 70–75. [https://doi.org/10.1016/S0921-5093\(02\)00057-6](https://doi.org/10.1016/S0921-5093(02)00057-6)
- Wang, Y. and Qin Q.-Z., A nanocrystalline NiO thin-film electrode prepared by pulsed laser ablation for Li-ion batteries, *J. Electrochem. Soc.*, 2002, vol. 149, no. 7, pp. A873–A878. <https://doi.org/10.1149/1.1481715>
- Zhu, G., Xi, C., Xu, H., Zheng, D., Liu, Y., Xu, X., and Shen, X., Hierarchical NiO hollow microspheres assembled from nanosheet-stacked nanoparticles and their application in a gas sensor, *RSC Adv.*, 2012, vol. 2, no. 10, pp. 4236–4241. <https://doi.org/10.1039/C2RA01307J>
- Kooti, M. and Matouri, L., A facile and mild method for synthesis of nickel oxide nanoparticles in the presence of various surfactants, *Res. Rev. J. Mater. Sci.*, 2014, vol. 2, no. 1, pp. 37–42. <https://doi.org/10.4172/2321-6212.1000118>
- Ju, D., Xu, H., Xu, Q., Gong, H., Qiu, Z., and Guo, J., High triethylamine-sensing properties of NiO/SnO<sub>2</sub> hollow sphere *p–n* heterojunction sensors, *Sens. Actuators B: Chem.*, 2015, vol. 215, pp. 39–44. <https://doi.org/10.1016/j.snb.2015.03.015>
- Arshak, K. and Gaidan, I., NiO/Fe<sub>2</sub>O<sub>3</sub> polymer thick films as room temperature gas sensors, *Thin Solid*

- Films*, 2006, vol. 495, nos. 1–2, pp. 286–291.  
<https://doi.org/10.1016/j.tsf.2005.08.298>
20. Darshane, S.L., Suryavanshi, S.S., and Mulla, I.S., Nanostructured nickel ferrite: A liquid petroleum gas sensor, *Ceram. Int.*, 2009, vol. 35, no. 5, pp. 1793–1797.  
<https://doi.org/10.1016/j.ceramint.2008.10.013>
  21. Chinnasamy, C.N., Narayanasamy, A., Ponpandian, N., Chattopadhyay, K., Shinoda, K., Jeyadevan, B., Tohji, K., Nakatsuka, K., Furubayashi, T., and Nakatani, I., Mixed spinel structure in nanocrystalline NiFe<sub>2</sub>O<sub>4</sub>, *Phys. Rev. B*, 2001, vol. 63, no. 18, 184108.  
<https://doi.org/10.1103/PhysRevB.63.184108>
  22. Albuquerque, A.S., Ardisson, J.D., Macedo, W.A.A., López, J.L., Paniago, R., and Persiano, A.I.C., Structure and magnetic properties of nanostructured Ni-ferrite, *J. Magn. Magn. Mater.*, 2001, vols. 226–230, pt. 2, pp. 1379–1381.
  23. Ortega, D., Kuznetsov, M.V., Morozov, Yu.G., Belousova, O.V., and Parkin, I.P., Thermal relaxation and collective dynamics of interacting aerosol-generated hexagonal NiFe<sub>2</sub>O<sub>4</sub> nanoparticles, *Phys. Chem. Chem. Phys.*, 2013, vol. 15, no. 48, pp. 20830–20838.  
<https://doi.org/10.1039/c3cp53981d>
  24. Madhusudan Reddy, K., Satyanarayana, L., Manorama, Sunkara V., and Misra, R.D.K., A comparative study of the gas sensing behavior of nanostructured nickel ferrite synthesized by hydrothermal and reverse micelle techniques, *Mater. Res. Bull.*, 2004, vol. 39, no. 10, pp. 1491–1498.  
<https://doi.org/10.1016/j.materresbull.2004.04.022>
  25. Satyanarayana, L., Madhusudan Reddy, K., and Manorama, S.V., Nanosized spinel NiFe<sub>2</sub>O<sub>4</sub>: A novel material for the detection of liquefied petroleum gas in air, *Mater. Chem. Phys.*, 2003, vol. 82, no. 1, pp. 21–26.  
[https://doi.org/10.1016/S0254-0584\(03\)00170-6](https://doi.org/10.1016/S0254-0584(03)00170-6)
  26. Chen, N.-S., Yang, X.-J., Liu, E.-S., Huanget, J.-L., Reducing gas-sensing properties of ferrite compounds MFe<sub>2</sub>O<sub>4</sub> (M=Cu, Zn, Cd and Mg), *Sens. Actuators B: Chem.*, 2000, vol. 66, no. 1–3, pp. 178–180.  
[https://doi.org/10.1016/S0925-4005\(00\)00368-3](https://doi.org/10.1016/S0925-4005(00)00368-3)
  27. Chen, D.-H. and He, X.-R., Synthesis of nickel ferrite nanoparticles by sol–gel method, *Mater. Res. Bull.*, 2001, vol. 36, nos. 7–8, pp. 1369–1377.  
[https://doi.org/10.1016/S0025-5408\(01\)00620-1](https://doi.org/10.1016/S0025-5408(01)00620-1)
  28. Liu, J., He, H., Jin, X., Hao, Z., and Xu, Z., Synthesis of nanosized nickel ferrites by shock waves and their magnetic properties, *Mater. Res. Bull.*, 2001, vol. 36, nos. 3–14, pp. 2357–2363.  
[https://doi.org/10.1016/S0025-5408\(01\)00722-X](https://doi.org/10.1016/S0025-5408(01)00722-X)
  29. Suematsu, H., Ishizaka, K., Kinemuchi, Y., Suzuki, T., Jiang, W., and Yatsui, K., Novel critical temperature resistor of sintered Ni–Fe–O nanosized powders, *J. Mater. Res.*, 2004, vol. 19, no. 4, pp. 1011–1014.  
<https://doi.org/10.1557/JMR.2004.0131>
  30. Ortega, D., Kuznetsov, M.V., Morozov, Y.G., Belousova, O.V., and Parkin, I.P., Phase, size and shape controlled formation of aerosol generated nickel and nickel oxide nanoparticles, *J. Alloys Compd.*, 2013, vol. 579, pp. 495–501.  
<https://doi.org/10.1016/j.jallcom.2013.06.128>
  31. Morozov, Y.G., Belousova, O.V., Kuznetsov, M.V., Ortega, D., and Parkin, I.P., Electric field-assisted levitation-jet aerosol synthesis of Ni/NiO nanoparticles, *J. Mater. Chem.*, 2012, vol. 22, no. 22, pp. 11214–11223.  
<https://doi.org/10.1039/c2jm31233f>
  32. Morozov, Y.G., Ortega, D., Belousova, O.V., Parkin, I.P., and Kuznetsov, M.V., Some peculiarities in the magnetic behavior of aerosol generated NiO nanoparticles, *J. Alloys Compd.*, 2013, vol. 572, pp. 150–157.  
<https://doi.org/10.1016/j.jallcom.2013.03.260>
  33. Krasnov, A.P., Morozov, Yu.G., and Chernov, E.A., Characteristic features of the vaporization mechanism in the crucible-free production of aerosol particles, *Powder Technol.*, 1994, vol. 81, no. 1, pp. 93–98.  
[https://doi.org/10.1016/0032-5910\(94\)02871-0](https://doi.org/10.1016/0032-5910(94)02871-0)
  34. Binions, R., Davies, H., Afonja, A., Dungey, S., Lewis, D., Williams, D.E., and Parkin, I.P., Zeolite-modified discriminating gas sensors, *J. Electrochem. Soc.*, 2009, vol. 156, no. 3, pp. J46–J51.  
<https://doi.org/10.1149/1.3065436>
  35. Peveler, W.J., Binions, R., Hailes, S.M.V., and Parkin, I.P., Detection of explosive markers using zeolite modified gas sensors, *J. Mater. Chem. A*, 2013, vol. 1, no. 17, pp. 2613–2620.  
<https://doi.org/10.1039/c2ta01027e>
  36. Tarttelin Hernández, P., Naik, A.J.T., Newton, E.J., Hailes, S.M.V., and Parkin, I.P., Assessing the potential of metal oxide semiconducting gas sensors for illicit drug detection markers, *J. Mater. Chem. A*, 2014, vol. 2, no. 23, pp. 8952–8960.  
<https://doi.org/10.1039/c4ta00357h>
  37. Costa, A.C.F.M., Lula, R.T., Kiminami, R.H.G.A., Gama, L.F.V., de Jesus, A.A., and Andrade, H.M.C., Preparation of nanostructured NiFe<sub>2</sub>O<sub>4</sub> catalysts by combustion reaction, *J. Mater. Sci.*, 2006, vol. 41, no. 15, pp. 4871–4875.  
<https://doi.org/10.1007/s10853-006-0048-1>
  38. Mironova-Ulmane, N., Kuzmin, A., Sildos, I., and Pärns, M., Polarization dependent Raman study of single-crystal nickel oxide, *Cent. Eur. J. Phys.*, 2011, vol. 9, no. 4, pp. 1096–1099.  
<https://doi.org/10.2478/s11534-010-0130-9>
  39. Tadic, M., Panjan, M., Markovic, D., Stanojevic, B., Jovanovic, D., Milosevic, I., and Spasojevic, V., NiO core–shell nanostructure with ferromagnetic-like behavior at room temperature, *J. Alloys Compd.*, 2014, vol. 586, suppl. 1, pp. S322–S325.  
<https://doi.org/10.1016/j.jallcom.2012.10.166>
  40. Anandha Babu, G., Ravi, G., Navaneethan, M., Arivanandhan, M., and Hayakawa, Y., An investigation of flower shaped NiO nanostructures by microwave and hydrothermal route, *J. Mater. Sci.: Mater. Electron.*, 2014, vol. 25, no. 12, pp. 5231–5240.  
<https://doi.org/10.1007/s10854-014-2293-4>
  41. Teoh, L.G. and Li, K.-D., Synthesis and characterization of NiO nanoparticles by sol–gel method, *Mater. Trans.*, 2012, vol. 53, no. 12, pp. 2135–2140.  
<https://doi.org/10.2320/matertrans.M2012244>
  42. Simmons, E.L., Diffuse reflectance spectroscopy: A comparison of the theories, *Appl. Opt.*, 1975, vol. 14, no. 6, pp. 1380–1386.  
<https://doi.org/10.1364/AO.14.001380>
  43. Rehman, S., Mumtaz, A., and Hasanain, S.K., Size effects on the magnetic and optical properties of CuO nanoparticles, *J. Nanopart. Res.*, 2011, vol. 13, no. 6, pp. 2497–2507.  
<https://doi.org/10.1007/s11051-010-0143-8>

44. Lin, H., Huang, C.P., Li, W., Ismat Shah, S., and Tseng, Y.-H., Size dependency of nanocrystalline TiO<sub>2</sub> on its optical property and photocatalytic reactivity exemplified by 2-chlorophenol, *Appl. Catal. B*, 2006, vol. 68, nos. 1–2, pp. 1–11.  
<https://doi.org/10.1016/j.apcatb.2006.07.018>
45. Tauc, J., Optical properties and electronic structure of amorphous Ge and Si, *Mater. Res. Bull.*, 1968, vol. 3, no. 1, pp. 37–46.  
[https://doi.org/10.1016/0025-5408\(68\)90023-8](https://doi.org/10.1016/0025-5408(68)90023-8)
46. Li, X., Zhang, X., Li, Z., and Qian, Y., Synthesis and characteristics of NiO nanoparticles by thermal decomposition of nickel dimethylglyoximate rods, *Solid State Commun.*, 2006, vol. 137, no. 11, pp. 581–584.  
<https://doi.org/10.1016/j.ssc.2006.01.031>
47. Madhu, G. and Biju, V., Nanostructured amorphous nickel oxide with enhanced antioxidant activity, *J. Alloys Compd.*, 2015, vol. 637, pp. 62–69.  
<https://doi.org/10.1016/j.jallcom.2015.02.157>
48. Adler, D. and Feinleib, J., Electrical and optical properties of narrow-band materials, *Phys. Rev. B*, 1970, vol. 2, no. 8, pp. 3112–3134.  
<https://doi.org/10.1103/PhysRevB.2.3112>
49. Biju, V., Ni 2p X-ray photoelectron spectroscopy study of nanostructured nickel oxide, *Mater. Res. Bull.*, 2007, vol. 42, no. 5, pp. 791–796.  
<https://doi.org/10.1016/j.materresbull.2006.10.009>
50. Grosvenor, A.P., Biesinger, M.C., Smart, R.St.C., and McIntyre, N.S., New interpretations of XPS spectra of nickel metal and oxides, *Surf. Sci.*, 2006, vol. 600, no. 9, pp. 1771–1779.  
<https://doi.org/10.1016/j.susc.2006.01.041>
51. Morozov, Y.G., Ortega, D., Belousova, O.V., Parkin, I.P., and Kuznetsov, M.V., Some peculiarities in the magnetic behavior of aerosol generated NiO nanoparticles, *J. Alloys Compd.*, 2013, vol. 572, pp. 150–157.  
<https://doi.org/10.1016/j.jallcom.2013.03.260>
52. Jaaniso, R. and Kian Tan, O., *Semiconductor Gas Sensors*, Oxford: Woodhead Publishing, 2013.
53. Gardner, J.W. and Bartlett, P.N., A brief history of electronic noses, *Sens. Actuators B: Chem.*, 1994, vol. 18, nos. 1–3, pp. 210–211.  
[https://doi.org/10.1016/0925-4005\(94\)87085-3](https://doi.org/10.1016/0925-4005(94)87085-3)
54. Korotcenkov, G. and Cho, B.K., Engineering approaches for the improvement of conductometric gas sensor parameters: 1. Improvement of sensor sensitivity and selectivity, *Sens. Actuators B: Chem.*, 2013, vol. 188, pp. 709–728.  
<https://doi.org/10.1016/j.snb.2013.07.101>
55. Vilaseca, M., Coronas, J., Cirera, A., Cornet, A., Morante, J.R., and Santamaria, J., Gas detection with SnO<sub>2</sub> sensors modified by zeolite films, *Sens. Actuators B: Chem.*, 2007, vol. 124, pp. 99–110.  
<https://doi.org/10.1016/j.snb.2006.12.009>
56. Bârsan, N. and Weimar, U., Understanding the fundamental principles of metal oxide based gas sensors: The example of CO sensing with SnO<sub>2</sub> sensors in the presence of humidity, *J. Phys.: Condens. Matter*, 2003, vol. 15, no. 20, R813.  
<https://doi.org/10.1088/0953-8984/15/20/201>
57. Sutka, A. and Gross, A., Spinel ferrite oxide semiconductor gas sensors, *Sens. Actuators B: Chem.*, 2016, vol. 222, pp. 95–105.  
<https://doi.org/10.1016/j.snb.2015.08.027>
58. Qureshi, A., Mergen, A., and Altindal, A., Preparation and characterization of Li and Ti codoped NiO nanocomposites for gas sensors applications, *Sens. Actuators B: Chem.*, 2009, vol. 135, no. 2, pp. 537–540.  
<https://doi.org/10.1016/j.snb.2008.09.029>
59. Deng, X., Zhang, L., Guo, J., Chen, Q., and Ma, J., ZnO enhanced NiO-based gas sensors towards ethanol, *Mater. Res. Bull.*, 2017, vol. 90, no. 6, pp. 170–174.  
<https://doi.org/10.1016/j.materresbull.2017.02.040>
60. Kim, H.-J. and Lee, J.-H., Highly sensitive and selective gas sensors using p-type oxide semiconductors: Overview, *Sens. Actuators B: Chem.*, 2014, vol. 192, no. 3, pp. 607–627.  
<https://doi.org/10.1016/j.snb.2013.11.005>
61. Wang, C., Cheng, X., Zhou, X., Sun, P., Hu, X., Shimanoe, K., Lu, G., and Yamazoe, N., Hierarchical  $\alpha$ -Fe<sub>2</sub>O<sub>3</sub>/NiO composites with a hollow structure for a gas sensor, *ACS Appl. Mater. Interfaces*, 2014, vol. 6, no. 15, pp. 12031–12037.  
<https://doi.org/10.1021/am501063z>
62. Yang, L., Xie, Y., Zhao, H., Wu, X., and Wang, Y., Preparation and gas-sensing properties of NiFe<sub>2</sub>O<sub>4</sub> semiconductor materials, *Solid State Electron.*, 2005, vol. 49, no. 6, pp. 1029–1033.  
<https://doi.org/10.1016/j.sse.2005.03.022>
63. Choi, J., Byun, J., and Sub, S., Influence of grain size on gas-sensing properties of chemiresistive p-type NiO nanofibers, *Sens. Actuators B Chem.*, 2016, vol. 227, pp. 149–156.  
<https://doi.org/10.1016/j.snb.2015.12.014>
64. Gadkari, A.B., Shinde, T.J., and Vasambekar, P.N., Ferrite gas sensors, *IEEE Sens. J.*, 2011, vol. 11, no. 4, pp. 849–861.  
<https://doi.org/10.1109/JSEN.2010.2068285>
65. Chu, X., Zhou, S., Zhang W., and Shui, H., Trimethylamine sensing properties of nano-LaFeO<sub>3</sub> prepared using solid state reaction in the presence of PEG400, *Mater. Sci. Eng. B*, 2009, vol. 164, no. 1, pp. 65–69.  
<https://doi.org/10.1016/j.mseb.2009.06.014>
66. Chu, X., Dongli, J., and Chenmou, Z., The preparation and gas-sensing properties of NiFe<sub>2</sub>O<sub>4</sub> nanocubes and nanorods, *Sens. Actuators B: Chem.*, 2007, vol. 123, no. 2, pp. 793–797.  
<https://doi.org/10.1016/j.snb.2006.10.020>
67. Feng, C., Ruan, S., Li, J., Zou, B., Luo, J., Chen, W., Dong, W., and Wu, F., Ethanol sensing properties of LaCo<sub>x</sub>Fe<sub>1-x</sub>O<sub>3</sub> nanoparticles: Effects of calcination temperature, co-doping and carbon nanotube treatment, *Sens. Actuators B: Chem.*, 2011, vol. 155, no. 1, pp. 232–238.  
<https://doi.org/10.1016/j.snb.2010.11.053>
68. Zhang, Y. and Zeng, W., New insight into gas sensing performance of nanoneedle-assembled and nanosheet-assembled hierarchical NiO nanoflowers, *Mater. Lett.*, 2017, vol. 195, pp. 217–219.  
<https://doi.org/10.1016/j.matlet.2017.02.124>